nature physics

ARTICLES

https://doi.org/10.1038/s41567-020-0807-y

Check for updates

Revealing the missing dimension at an exceptional point

Hua-Zhou Chen[1,2,11], Tuo Liu[3,4,11], Hong-Yi Luan[1,2,11], Rong-Juan Liu[5], Xing-Yuan Wang[6], Xue-Feng Zhu[7], Yuan-Bo Li[1], Zhong-Ming Gu[3], Shan-Jun Liang[3,4], He Gao[3], Ling Lu[5], Li Ge[8,9]✉, Shuang Zhang[10], Jie Zhu[3,4]✉ and Ren-Min Ma[1,2]✉

The radiation of electromagnetic and mechanical waves depends not only on the intrinsic properties of the emitter but also on the surrounding environment. This principle has laid the foundation for the development of lasers, quantum optics, sonar, musical instruments and other fields related to wave–matter interaction. In the conventional wisdom, the environment is defined exclusively by its eigenstates, and an emitter radiates into and interacts with these eigenstates. Here we show experimentally that this scenario breaks down at a non-Hermitian degeneracy known as an exceptional point. We find a chirality-reversal phenomenon in a ring cavity where the radiation field reveals the missing dimension of the Hilbert space, known as the Jordan vector. This phenomenon demonstrates that the radiation field of an emitter can become fully decoupled from the eigenstates of its environment. The generality of this striking phenomenon in wave–matter interaction is experimentally confirmed in both electromagnetic and acoustic systems. Our finding transforms the fundamental understanding of light–matter interaction and wave–matter interaction in general, and enriches the intriguing physics of exceptional points.

In electromagnetics, the canonical paradigm to consider the radiation process is built on the notion that an emitter interacts with the photonic eigenstates of its surrounding environment. This approach demonstrated its profound power in the understanding of spontaneous emission, which is a fundamental phenomenon associated with the generation of light and plays an essential role in the development of modern quantum mechanics[1–12]. According to the theory pioneered by Weisskopf and Wigner[1], spontaneous emission is induced by the zero-point energy of the vacuum photon field. This concept was further developed by Purcell, who revealed that the rate of spontaneous emission relies on the interaction of the emitter with the photonic eigenstates of its surrounding environment[2]. Over the past decades, various systems including dielectric structures, photonic crystals, plasmonics and metamaterials have been developed to construct desired photonic states and control light–matter interaction, leading to applications including low-threshold lasers, efficient single-photon sources, high-precision measurements, quantum information processing and so on[4–12].

In like manner, a striking puzzle in the propagation of sound was solved by Lord Rayleigh at the beginning of the nineteenth century[13]. The aforementioned paradigm in electromagnetics also revealed the acoustic whispering-gallery mode (WGM) that enhances human voices inside St Paul's cathedral in London, whose role Lord Rayleigh also contemplated in the propagation of earthquake disturbances. In fact, the same notion regarding the source of a mechanical wave and its surrounding vibrational modes has laid down the foundation to study, conceive and realize a wide range of dynamic behaviours. From architectural acoustics and musical instruments to sonar, ultrasonography and surface acoustic wave functional devices, many breakthroughs have been enabled by the evolving understanding of this paradigm[14].

However, the notion that the photonic or mechanical environment is determined exclusively by its eigenstates came under scrutiny in non-Hermitian systems with quantum-inspired symmetries, including those obeying the so-called parity–time (PT) symmetry[15–27]. PT-symmetric Hamiltonians can undergo a phase transition from the PT-symmetric phase, with an entirely real spectrum, to the spontaneously broken regime, where eigenvalues appear as complex conjugate pairs[24]. In addition, a singularity known as an exceptional point or non-Hermitian degeneracy arises at the symmetry-breaking point[28–31]. At an exceptional point, two or more eigenstates become identical and so do their eigenvalues. As a result, the eigenstates do not span the entire Hilbert space at an exceptional point, with one or more dimensions missing. Mathematically, these missing dimensions are supplemented by the Jordan vectors[32,33]. While this property, unique to non-Hermitian systems, has been known for decades, dating back to the study of nuclear decay[34], the wave functions of these missing dimensions have not been observed in any physical system.

Utilizing the radiation of a single emitter in a PT-symmetric ring cavity, here we experimentally reveal the wave function of the missing dimension at an exceptional point in both electromagnetic and mechanical systems. Our observation presents the striking fact that the radiation field can become fully decoupled from the eigenstates of the environment, which fundamentally transforms our understanding of the emission process. Furthermore, we show in

[1]State Key Lab for Mesoscopic Physics and School of Physics, Peking University, Beijing, China. [2]Frontiers Science Center for Nano-optoelectronics & Collaborative Innovation Center of Quantum Matter, Beijing, China. [3]Department of Mechanical Engineering, Hong Kong Polytechnic University, Hong Kong SAR, China. [4]Hong Kong Polytechnic University Shenzhen Research Institute, Shenzhen, China. [5]Institute of Physics, Chinese Academy of Sciences/Beijing National Laboratory for Condensed Matter Physics, Beijing, China. [6]College of Mathematics and Physics, Beijing University of Chemical Technology, Beijing, China. [7]School of Physics and Innovation Institute, Huazhong University of Science and Technology, Wuhan, Hubei, China. [8]Department of Physics and Astronomy, College of Staten Island, CUNY, Staten Island, NY, USA. [9]Graduate Center, CUNY, New York, USA. [10]School of Physics and Astronomy, University of Birmingham, Birmingham, UK. [11]These authors contributed equally: Hua-Zhou Chen, Tuo Liu, Hong-Yi Luan. ✉e-mail: li.ge@csi.cuny.edu; jiezhu@polyu.edu.hk; renminma@pku.edu.cn

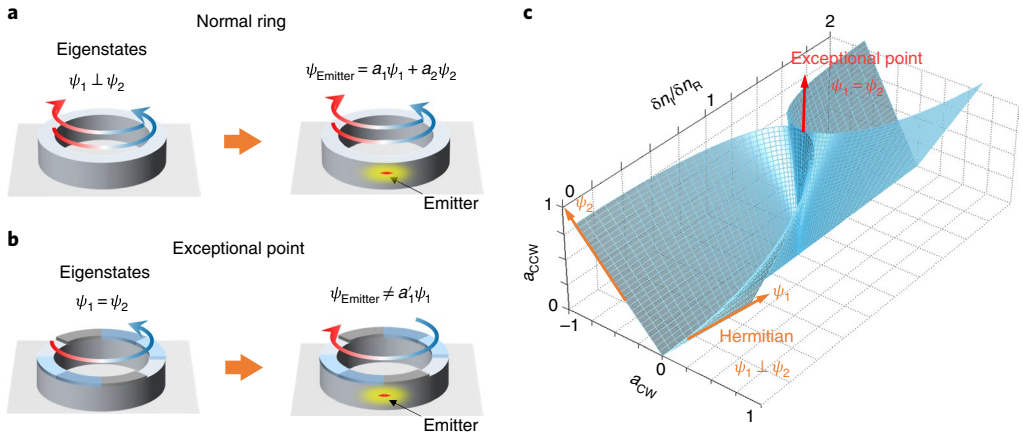

Fig. 1 | Chirality-reversal radiation at an exceptional point. a, Schematic of a normal ring cavity with uniform refractive index, which supports two counterpropagating eigenstates (left). A single emitter at the resonant frequency will excite both eigenstates, forced by the completeness and orthogonality of the eigenbasis (right). **b**, Schematic of a ring cavity operating at an exceptional point, where the two eigenstates coalesce (left). A single emitter can become fully decoupled from the coalesced eigenstate and radiate to the missing dimension with the opposite handedness (right). **c**, Evolution of the directions of the two eigenstates $\psi_{1,2} = \begin{pmatrix} a_{CW} \\ a_{CCW} \end{pmatrix}$ of a PT-symmetric ring cavity as a function of $\delta n_I/\delta n_R$. At $\delta n_I/\delta n_R = 0$, the two eigenstates are orthogonal; they coalesce when $\delta n_I/\delta n_R = 1$. Note that for $\delta n_I/\delta n_R > 1$ the horizontal axis changes from a_{CW} to ia_{CW}.

the experiment that the resulting radiation field displays completely opposite chirality to the coalesced eigenstate, leading to vortex emission in the far field carrying a non-zero orbital angular momentum (OAM). The anomalous wave–matter interaction effect, the device design scheme and the methodology we demonstrate in our work will contribute to a broad range of research fields, including non-Hermitian physics, photonics and acoustics as well as chiral quantum optics.

General theoretical analysis

We first present a general theoretical analysis based on coupled-mode equations to show that at an exceptional point the radiation field of an emitter can become fully decoupled from the eigenstates of its environment. Let us briefly review the interaction of a single emitter with a normal ring cavity. At a given cavity resonant frequency, the eigenstates with a non-zero OAM are doubly degenerate with two counterpropagating directions, one travelling clockwise (CW) and the other counterclockwise (CCW). Their wave functions are proportional to $e^{il\varphi}$ and $e^{-il\varphi}$, where l and $-l$ are their OAMs and φ is the azimuthal angle. We will refer to them also as left-handed and right-handed WGMs. When a single emitter radiates at this resonant frequency inside the cavity, both eigenstates will be excited, which is forced by the completeness and orthogonality of the eigenbasis (Fig. 1a).

Now consider a ring cavity operating at an exceptional point by introducing a PT-symmetric refractive index modulation $(n(\varphi) = n_0 + \delta n_R \cos(2l\varphi) - i\,\delta n_I \sin(2l\varphi))$ along the azimuthal direction (Fig. 1b), where n_0 is the background refractive index, and δn_R and δn_I are real and imaginary parts of the refractive index modulation, respectively. The coupled-mode equations of the system can be written as

$$\frac{d}{dt}\begin{pmatrix} a_{CW} \\ a_{CCW} \end{pmatrix} = \begin{pmatrix} i\omega - \gamma_{tot} & \chi_{ab} \\ \chi_{ba} & i\omega - \gamma_{tot} \end{pmatrix}\begin{pmatrix} a_{CW} \\ a_{CCW} \end{pmatrix} \equiv i\mathcal{H}\begin{pmatrix} a_{CW} \\ a_{CCW} \end{pmatrix} \quad (1)$$

In equation (1), a_{CW} (a_{CCW}) is the complex amplitude of the CW (CCW) wave, and ω and γ_{tot} are the resonant frequency and total decay rate of the unperturbed counterpropagating WGMs in the non-Hermitian Hamiltonian $\mathcal{H}$. $\chi_{ab(ba)} \propto (\delta n_R \mp \delta n_I)$ are the coupling strengths from the CCW mode to the CW mode and vice versa (Supplementary Section 1). The system operates at an exceptional point when $|\delta n_R| = |\delta n_I|$, that is, the coupling between the two WGMs becomes unidirectional with either χ_{ab} or χ_{ba} vanishing, indicating that the back-reflections induced by the real and imaginary parts of the index modulation $\delta n_{R,I}$ interfere with each other in a completely destructive way for the CCW or CW wave. In this scenario, the Hamiltonian becomes a defective matrix with a single coalesced eigenstate ψ_{EP}. In Fig. 1c, we show the evolution of the two eigenstates as a function of $\delta n_I/\delta n_R$. At $\delta n_I/\delta n_R = 1$, the two eigenstates become identical, that is, the unidirectional CCW mode $\psi_{EP} = \begin{pmatrix} 0 \\ 1 \end{pmatrix}$, and the two-dimensional Hilbert space coalesces to a one-dimensional space.

At this exceptional point, a surprising phenomenon emerges when we introduce a single emitter to interact with the cavity: the radiation field of the emitter can become fully decoupled from the eigenstate. Instead, it couples to the missing dimension of the Hilbert space, that is, the Jordan vector $\mathbf{J} \propto \begin{pmatrix} 1 \\ 0 \end{pmatrix}$ defined by $(\mathcal{H} - \omega\mathbf{1})\mathbf{J} = \psi_{EP}$, displaying the opposite handedness to the coalesced eigenstate (Fig. 1b). Considering a coupled-mode theory with an excitation source from a single emitter (Supplementary Section 2), the amplitude ratio of CCW to CW waves in the radiation field can be derived as

$$\frac{a_{CCW}}{a_{CW}} = 1 - \frac{\chi_{ba}(\varphi_0)}{i\Delta - \gamma_{tot}} \quad (2)$$

where Δ is the detuning between the emitter oscillation frequency and cavity resonant frequency and $\chi_{ba}(\varphi_0)$ is the position-dependent coupling constant of the emitter-excited CW mode to the CCW mode (Supplementary Section 2). Due to the presence of γ_{tot}, a_{CCW}/a_{CW} cannot be infinite, indicating that we cannot obtain a pure CCW wave, that is, the coalesced eigenstate at the exceptional point. When on resonance ($\Delta = 0$), the ratio vanishes at $\gamma_{tot} = -\chi_{ba}(\varphi_0)$, which is the condition we have employed to observe a pure Jordan vector at an exceptional point. In our conducted experiments, this is satisfied with the requirements of $|\chi_{ba}(\varphi_0)| = \gamma_{tot}$ and $\varphi_0 = \pi/4l$. The analysis from the coupled-mode equations provides us with an intuitive physical picture to understand the

chirality-reversal radiation via completely destructive interference between the directly radiated and the backscattered CCW waves. At $\gamma_{tot}=-\chi_{ba}(\varphi_0)$, the emitter's position of $\varphi_0=\pi/4l$ is a result of the requirement of the destructive interference condition, while the requirement of $|\chi_{ba}(\varphi_0)|=\gamma_{tot}$ ensures that the amplitude of the reflected field accumulates and finally reaches the same value as the direct emitted CCW mode (Supplementary Section 3).

We note that the chirality-reversal phenomenon is in stark contrast to exceptional point lasers, where the properties extracted are solely determined by the chiral eigenstates, and not the Jordan vectors. When the emitter position deviates from $\varphi_0=\pi/4l$, the interference condition will change accordingly. In exceptional point lasers, the emitters are distributed over the entire cavity, and therefore the chirality of the lasing mode is determined by the integrated radiation of all emitters. On the basis of the steady-state ab initio laser theory (SALT)[35,36], we find that a uniform gain profile leads to lasing in the coalesced eigenstate, but not in the Jordan vector (Supplementary Section 4).

To further validify the analysis based on coupled-mode equations, we employ the Green's function to illustrate why the single emitter radiates with the opposite handedness to the coalesced eigenstate near and at an exceptional point. We note that, even though electromagnetic and acoustic waves are different in several fundamental perspectives, for example, with the latter being a longitudinal wave and depending on the thermal dynamical properties of a needed propagation medium, both of them can be described by the wave equation and a refractive index. Consequently, when the polarization of an electromagnetic mode is unimportant, the respective electromagnetic and acoustic modes can be defined using the Helmholtz equation. To capture their interaction with a single emitter in a PT-symmetric ring cavity with a radius r_R, we use the corresponding Green's function defined by

$$\left[\frac{1}{r_R^2}\partial_\varphi^2+n^2(\varphi)k^2\right]G(\varphi,\varphi_0;k)=\frac{1}{r_R}\delta(\varphi-\varphi_0) \tag{3}$$

where k is the free-space wave vector, and $\delta(\varphi-\varphi_0)$ is a delta function at the source position φ_0. If the quality factor of this CCW chiral mode is high, then the radiation of a point source embedded inside the cavity is expected to follow the pattern of the CCW chiral mode on resonance at the exceptional point, which can be seen from the bilinear expansion of the Green's function:

$$G(\varphi,\varphi_0;k)\equiv\sum_m\alpha_m\psi_m(\varphi)=\sum_m\frac{\psi_m(\varphi)\psi_m(\varphi_0)}{(k^2-\tilde{k}_m^2)(m,m)}\overset{k\to\tilde{k}_l}{\longrightarrow}\frac{\psi_l(\varphi)\psi_l(\varphi_0)}{(k^2-\tilde{k}_l^2)(l,l)} \tag{4}$$

where $\psi_m(\varphi)$ and $\tilde{k}_m^2$ are respectively the eigenstates and eigenvalues defined by $\left[\frac{1}{r_R^2}\partial_\varphi^2+n^2(\varphi)\tilde{k}_m^2\right]\psi_m(\varphi)=0$, and (m,m) denotes the non-Hermitian inner product (Supplementary Section 4). However, this expectation following the conventional wisdom does not hold here, as indicated by the diverging right-hand side of equation (4) at the exceptional point: the denominator vanishes (that is, $(l,l)=0$) due to the coalescence of the two eigenstates. To resolve these issues, we start from a system slightly deviated from the exceptional point ($\delta n_I/\delta n_R\equiv 1-\varsigma^2$) and then take the limit $\varsigma\to 0$ towards the exceptional point at $\delta n_I/\delta n_R=1$. By omitting the off-resonance modes in equation (4), we approximate the Green's function by the summation of the two almost identical eigenstates near the exceptional point, which are expressed in terms of CCW and CW waves themselves. We then insert it in equation (3) and drop the higher-harmonic terms in the product $n^2(\varphi)\psi_m(\varphi)$, which gives the Green's function:

$$G(\varphi,\varphi_0;k)\propto e^{il(\varphi-\varphi_0)}+\left(1+\frac{\delta n_R}{in_I}e^{-2il\varphi_0}\right)e^{-il(\varphi-\varphi_0)} \tag{5}$$

to leading order in ς,where n_I is the imaginary part of the refractive index characterizing γ_{tot}. The reciprocity of the Green's function can be easily checked despite the non-Hermitian nature of the system. It is important to note that this expression for the Green's function is independent of ς, and hence it can be applied to the exceptional point as well. Strikingly, it indicates that the emitter's radiation can become completely decoupled from the coalesced eigenstate, which happens when $1+\frac{\delta n_R}{in_I}e^{-2il\varphi_0}=0$. Note that this requirement is equivalent to the one we derived from coupled-mode equations. As a result, the Green's function (and hence the total radiation field) is unidirectional, following the Jordan vector in the CW direction, which completely reverses the chirality of the CCW ring resonance at the exceptional point.

Experimental verification in an electromagnetic system

To construct the aforementioned exceptional point in an electromagnetic system, we employ a PT-symmetric coaxial microwave cavity to construct the exceptional point, where germanium ridges and air grooves are used to modulate the imaginary and real parts of the refractive index, respectively (Fig. 2a and Supplementary Section 5). Note that the structure we constructed to interact with a single emitter is passive (that is, without gain), but still effectively PT symmetric. The cavity field is described by equation (1), and in the experiment we tune the PT-symmetric modulation to $\delta n_R=\delta n_I$ ($\chi_{ab}=0$) to reach an exceptional point, giving rise to the coalesced CCW eigenstate with OAM $|l|=1$ (Fig. 2b and Supplementary Sections 1 and 6).

To investigate the interaction of a single emitter with the coaxial cavity at the exceptional point, a dipole antenna is employed as a single source and inserted into the fabricated cavity (Fig. 2c,d and Methods). The radiation of a dipole antenna is governed by its photonic environment as in the spontaneous emission, while a subtle difference lies in the radiation rate[37]. Another dipole antenna is used to probe the radiation field 22 mm above the upper surface of the cavity, which leaks out through a ring opening (Fig. 2c and Supplementary Section 7). The height of the cavity itself is 21 mm, and the resonant frequency at the exceptional point is around 8.212 GHz. Red lines in Fig. 2e,f show the measured phase and amplitude of the radiation field when the excitation antenna is placed at the centre of the loss region ($\varphi_0=\pi/4$). There are two remarkable features of the radiation field. First, the phase increases linearly from $-\pi$ to π and the amplitude remains almost unchanged, which directly illustrates that the radiation field of the single-dipole emitter is a travelling wave inside the cavity. In comparison, the antenna excites a standing wave in the control experiment of a normal ring cavity without PT-symmetric modulation, showing two amplitude nodes and the corresponding π phase jump at each node (blue curves in Fig. 2e,f). Second, the phase evolution of the radiation field indicates that it is a left-handed wave ($\sim e^{il\varphi}$), that is, it displays the opposite handedness to the coalesced right-handed eigenstate ($\sim e^{-il\varphi}$) at the exceptional point.

Therefore, the chirality-reversal radiation provides direct observation of the wave function associated with the Jordan vector. It also reveals that the emitter can become fully decoupled from the eigenstates of the system, which is fundamentally different from previously reported chiral optical devices at an exceptional point (Supplementary video and Supplementary Section 4), where only the properties of the coalesced eigenstate are considered and observed[38–43]. We also note that, when considering the time evolution of an initial state at an exceptional point without the emitter, the asymptotic wave function is given only by the coalesced eigenstate, even when the initial input state is the Jordan vector[44,45].

The radiation of the single-emitter-excited exceptional point cavity is a vortex beam carrying OAM (Fig. 3a). Figure 3b shows the measured amplitude and phase of the cavity radiation field. The spiral phase pattern and the intensity singularity due to the

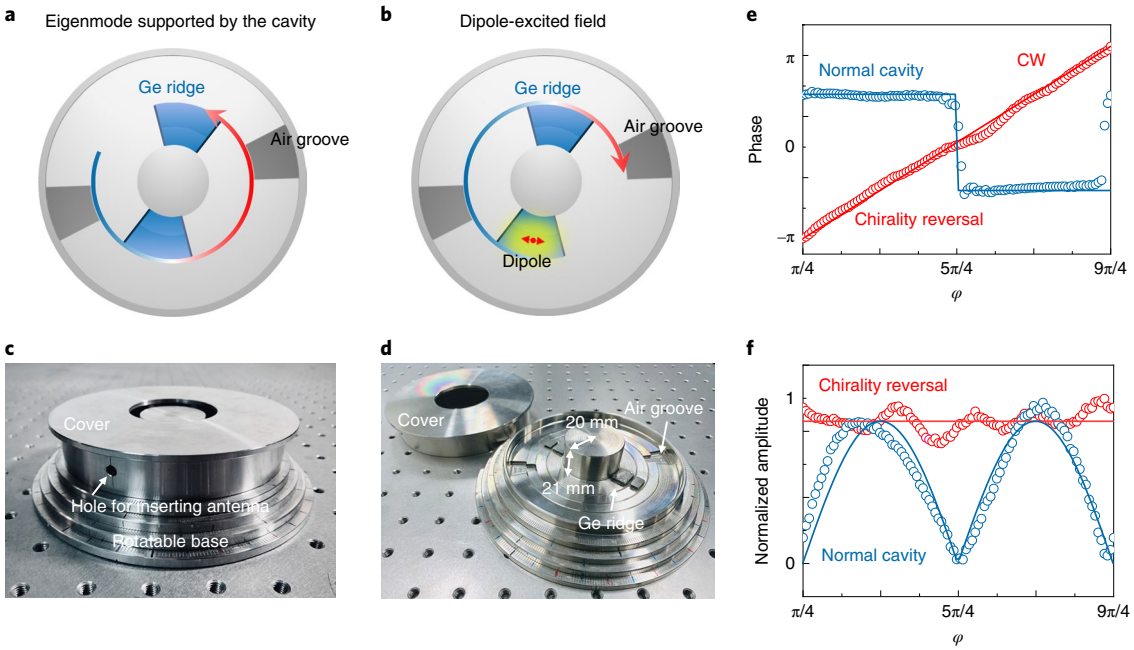

Fig. 2 | Experimental results of chirality-reversal radiation. a,**b**, Eigenstate (**a**) and single-emitter radiation field (**b**) of an exceptional point cavity. To construct an exceptional point, a PT-symmetric refractive index modulation is introduced into a ring cavity as air grooves and germanium ridges. **c**,**d**, Experimentally fabricated exceptional point cavity with the cover in closed (**c**) and open (**d**) configurations. **e**,**f**, Phase (**e**) and amplitude (**f**) of the single-emitter radiation field as a function of φ. As a comparison, the single-emitter radiation field of a normal ring cavity is also presented. Circles: experiment. Solid lines: theory.

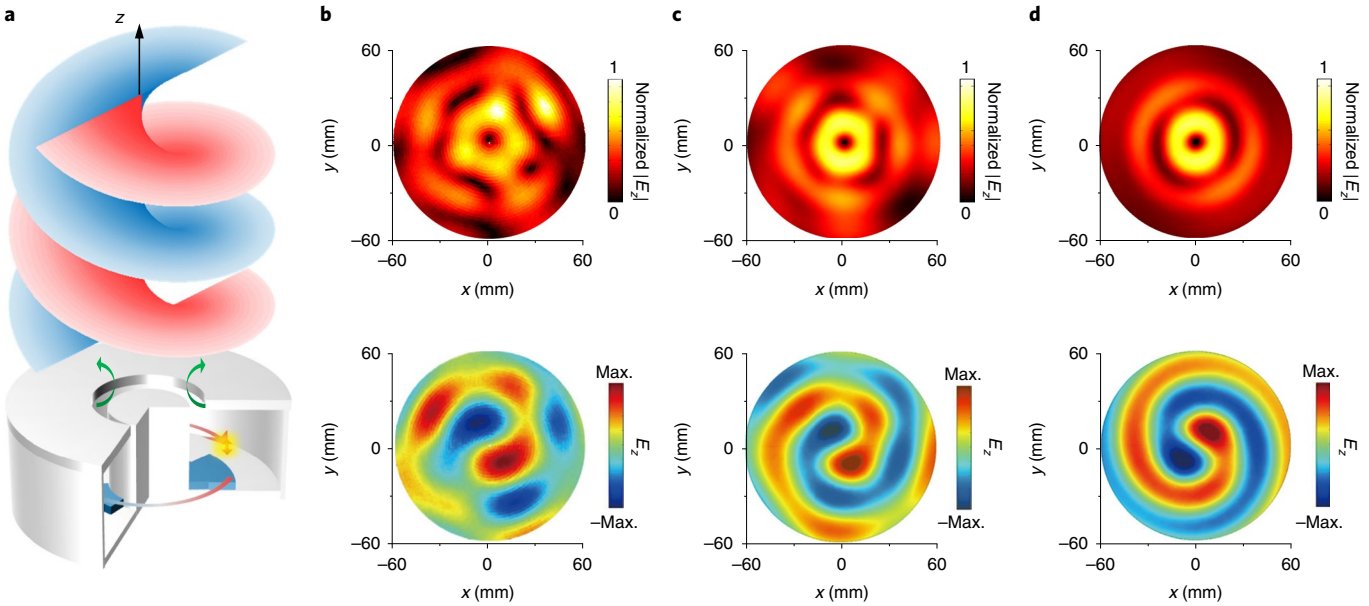

Fig. 3 | Chirality-reversal vortex radiation from a single emitter. a, Schematic of the vortex radiation from a single emitter inside the exceptional point cavity. The radiation leaks out through a narrow ring opening on the cover of the cavity. **b**,**c**, Top row: experimental (**b**) and simulated (**c**) $|E_z|$ fields of the vortex radiation 22 mm above the cavity. Bottom row: the corresponding experimental and simulated E_z fields. **d**, Simulated $|E_z|$ and E_z fields of the coalesced eigenstate of the cavity. Clearly, the single-emitter-excited vortex radiation presents opposite handedness to the eigenstate.

undefined phase at the centre show clearly the signatures of a vortex beam with a topological charge of −1, and they match well with the simulation results (Fig. 3c). As a comparison, Fig. 3d shows the simulated amplitude and phase of the coalesced cavity eigenstate, which has the opposite handedness. The vortex nature and topological charge of the radiation field are also verified by observing at different heights above the cavity (Supplementary Section 8).

Our system not only provides new understanding of light–matter interaction but also introduces a new means of control to manipulate the radiation field at the single-emitter level. This functionality

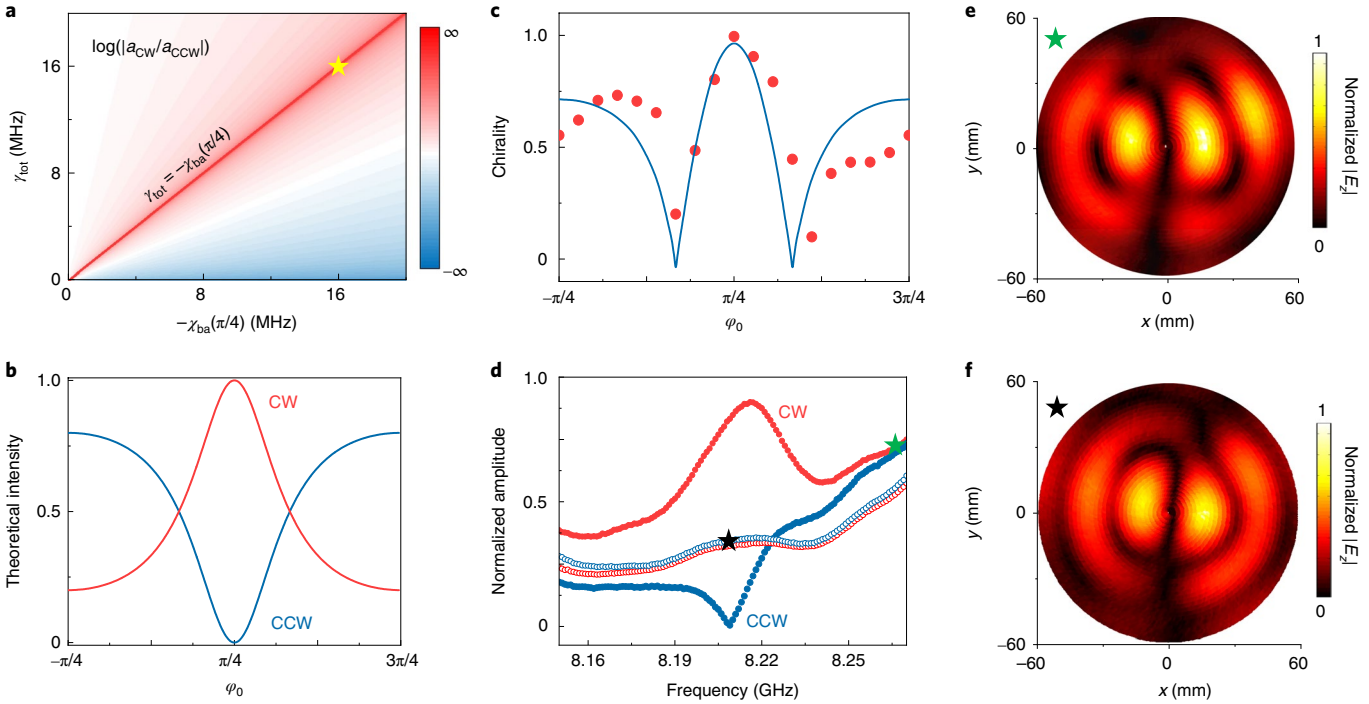

Fig. 4 | Position- and frequency-dependent chirality of single-emitter radiation inside the exceptional point cavity. a, Amplitude ratio between the right-handed and left-handed waves of the single-emitter radiation field in the parameter space of γ_{tot} and $\chi_{ba}(\pi/4)$. The yellow star indicates the experimental condition. **b**, Position-dependent left-handed and right-handed wave excitation of a single emitter inside the exceptional point cavity at $|\chi_{ba}(\varphi_0)| = \gamma_{tot}$. **c**, Position-dependent chirality of a single-emitter radiation field inside the exceptional point cavity at $|\chi_{ba}(\varphi_0)| = \gamma_{tot}$. Circles: experiment. Solid line: theory. **d**, Frequency-dependent left-handed and right-handed wave excitation of a single emitter inside the exceptional point cavity (filled circles) and the normal cavity (open circles). **e**, $|E_z|$ field distribution of the excited field in the conditions indicated by the green star in **d**. **f**, $|E_z|$ field distribution of the excited field in the conditions indicated by the black star in **d**. Both **e** and **f** exhibit nodes in the azimuthal direction, indicating the excitation of a standing wave with zero OAM.

is achieved via the position- and frequency-dependent chirality of the dipole-excited field (Fig. 4). Here the chirality is defined as[12,46] $\zeta = 1 - \frac{\min\left[|a_{CW}|^2, |a_{CCW}|^2\right]}{\max\left[|a_{CW}|^2, |a_{CCW}|^2\right]}$. The experimentally obtained chirality can reach a value as high as 0.995 at $\varphi_0 = \pi/4$ (Fig. 4c). Figure 4d shows the amplitudes of the dipole-excited left-handed and right-handed fields as functions of the excitation frequency. The left-handed (right-handed) field reaches its maximum (minimum) near the resonant frequency. The contrast between left-handed and right-handed fields decreases as the frequency detuning increases, which is consistent with our theoretical prediction. Figure 4e shows the field distribution of the exceptional point cavity excited at a frequency far away from resonance, and Fig. 4f shows the field distribution of the normal ring cavity excited at the resonant frequency. Both patterns are standing waves corresponding to zero chirality.

Experimental verification in an acoustic system

We have also observed the excitation of the Jordan vector and the associated chirality-reversal phenomenon in a mechanical wave system with a passive acoustic PT-symmetric ring cavity. The fabricated sample consists of a closed ring cavity with a rectangular cross-section with $a = 25$ mm and $b = 50$ mm (Fig. 5a). The inner and outer radii are 40 mm and 65 mm, respectively. The background acoustic refractive index for the fundamental mode inside the ring cavity is experimentally determined to be $1.0047 - i0.0038$ (relative to the acoustic refractive index of air; Supplementary Section 9). The complex acoustic index modulation, whose amplitudes $\delta n_R = \delta n_I \approx 0.0278$ are obtained from the chirality-reversal condition, is realized by modifying the boundary condition of the cavity's corresponding inner-wall regions with artificially constructed metastructures. The periodic metagrooves provide capacitive boundaries to achieve slow sound, and the microperforated cavity walls yield resistive boundaries to tailor the loss (Supplementary Sections 10 and 11). The point sound source (monopole) is implemented by embedding a balanced armature, emitting acoustic waves into the passive PT-symmetric ring cavity. As for the electromagnetic experiment, the centre of the loss region ($\varphi_0 = \pi/4$) corresponds to the chirality-reversal condition.

The simulated and measured acoustic fields evidently validate our theoretical prediction and are consistent with the results obtained in the electromagnetic wave system. As shown in Fig. 5b, the introduction of a balanced passive PT-symmetric modulation alters the eigenstates of a normal ring cavity from a pair of counter-propagating modes to a coalesced CCW mode. The resultant chirality, denoted by the acoustic intensity vectors (black cones in Fig. 5b), can be represented by the continuous phase decrement from π to $-\pi$. As anticipated, the monopole sound source positioned at $\varphi_0 = \pi/4$ does not excite the CCW mode. Instead, it generates a WGM with reversed chirality to the cavity's eigenmode, as depicted by the black cones in Fig. 5c. Consequently, the interference pattern nearly disappears in Fig. 5d, and the phase varies quasilinearly from $-\pi$ to π in Fig. 5e, in stark contrast to the standing-wave field inside a normal cavity without PT-symmetric index modulation (blue lines and circles in Fig. 5d,e).

With the information experimentally retrieved from the standing-wave ratio and phase gradient, it can be seen in Fig. 6a,b that the chirality of the excited acoustic wave evolves continuously with respect to the azimuthal sound source position φ_0. When $\pi/12 < \varphi_0 < 5\pi/12$, the excited sound field is in the opposite direction to the eigenmode. It becomes completely reversed as φ_0 approaches $\pi/4$, which produces an almost linearly increased phase distribution (Fig. 6c). At $\varphi_0 = \pi/12$ or $5\pi/12$, the CCW and CW modes

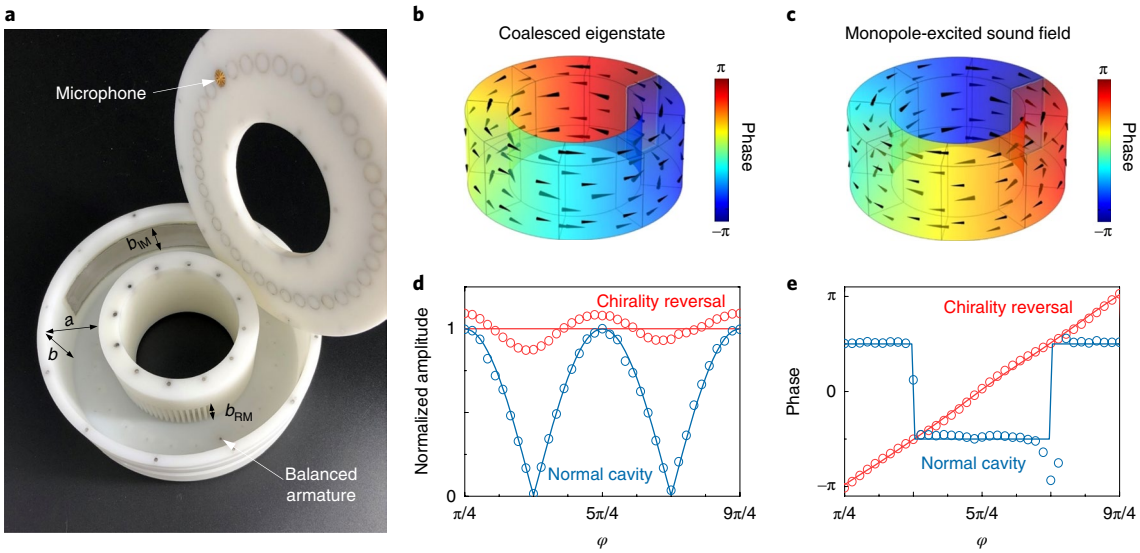

Fig. 5 | Experimental demonstrations of the chirality-reversal phenomenon in an acoustic wave system. a, Photograph of the passive acoustic PT-symmetric ring cavity ($l=1$). The cavity's inner and outer radii are 40 mm and 65 mm, respectively. For the cross-section, $a=25$ mm and $b=50$ mm. The real-part modulation is realized by decorating metagrooves on the inner wall with $b_{RM}=29$ mm; the imaginary part modulation is done by introducing leakages via the microperforated plates with $b_{IM}=9.1$ mm (Methods). The resonant frequency at the exceptional point is about 1,040 Hz. **b**,**c**, Eigenstate (**b**) and excited sound field (**c**) in the passive PT-symmetric ring cavity. Black cones: acoustic intensity vectors. **d**,**e**, Measured and simulated pressure amplitude (**d**) and phase (**e**) distributions of the passive PT-symmetric ring cavity. As a comparison, the single-emitter radiation field of a normal acoustic ring cavity is also presented. Circles: experiment. Solid lines: theory.

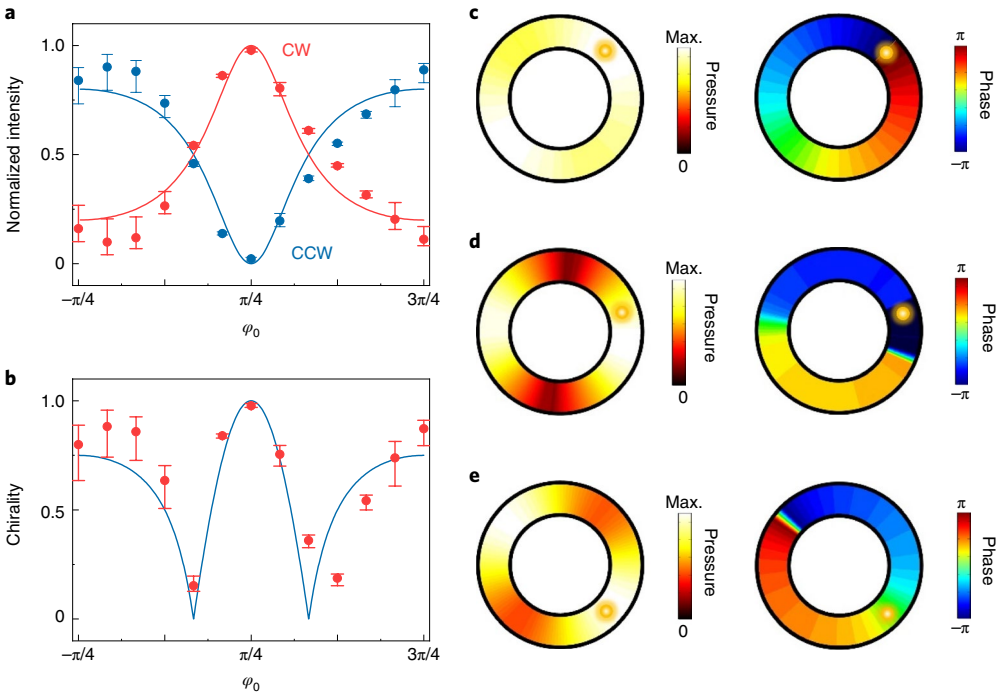

Fig. 6 | Chirality evolution in the passive acoustic PT-symmetric system. a,**b**, Position-dependent left/right-handed mode intensity (**a**) and chirality (**b**) of a monopole radiation field inside the exceptional point cavity at $|\chi_{ba}(\varphi_0)| = \gamma_{tot}$. The error bars denote the range of data variability from the mean values (data points) of three independent measurements. Circles: experiment. Solid lines: theory. **c**–**e**, Measured sound fields inside the ring cavity for different source positions (**c**, $\varphi_0=\pi/4$; **d**, $\varphi_0=\pi/12$; **e**, $\varphi_0=-\pi/4$). Left column: normalized pressure amplitude. Right column: phase. The bright spots denote the source position.

have equal amplitudes and form a standing-wave field (Fig. 6d). After the azimuthal source position moves to $-\pi/4 \leq \varphi_0 < 5\pi/12$ or $5\pi/12 < \varphi_0 \leq 3\pi/4$, the CCW mode outweighs the CW mode, so the chirality is in the same direction as the eigenmode (Fig. 6e). Such a chirality-reversal behaviour of sound suggests an additional degree of freedom, namely, the interplay between excitation source and

eigenstates, hidden behind non-Hermitian degeneracies, since the studied passive acoustic PT-symmetric system consistently operates at a fixed exceptional point during the whole evolution process. Our demonstration of chirality reversal in the acoustic system provides a new path towards highly efficient and controllable generation of acoustic OAM with a single source, essential for many applications ranging from topological acoustics[47,48] to particle manipulation and high-speed acoustic communication[49,50]. On the other hand, with their unique capabilities and flexibilities such as zero cutoff in a rigid waveguide and extremely low dispersion in air, acoustic wave systems[51–53] have been gaining momentum as a distinctive and effective classical wave platform for experimental exploration of non-Hermitian physics.

Conclusions

In summary, we have revealed experimentally a surprising phenomenon of chirality-reversal radiation at an exceptional point, which provides a direct observation of the wave function associated with the Jordan vector, that is, the missing dimension of the Hilbert space. It also shows that the radiation field of an emitter can become fully decoupled from the eigenstates of its environment. Based on the chirality-reversal mechanism, we have further demonstrated vortex radiation with a tunable chirality. While there are various methods to generate optical vortices by directly modulating either laser cavities or the laser emission beam[54,55], twisting the radiation of a single emitter directly into a vortex beam remains a formidable task. A promising approach that has been demonstrated in the emerging chiral quantum optics employs spin-momentum locking, which however requires a circularly polarized dipole emitter[12,56,57]. Here, instead, we have constructed a chiral vacuum field to twist the radiation of an embedded dipole with a simple linear polarization, which provides a new paradigm for chiral quantum optics at the nanoscale. Our experimental demonstrations are conducted in both electromagnetic and mechanical systems, which shows the generality of this striking phenomenon in wave–matter interaction. Therefore, our finding enriches the understanding of the intriguing physics at an exceptional point, which we believe will have a broad influence on research fields including non-Hermitian physics, photonics and acoustics as well as chiral quantum optics.

Online content

Any methods, additional references, Nature Research reporting summaries, source data, extended data, supplementary information, acknowledgements, peer review information; details of author contributions and competing interests; and statements of data and code availability are available at https://doi.org/10.1038/s41567-020-0807-y.

Received: 16 September 2019; Accepted: 21 January 2020;
Published online: 9 March 2020

References

1. Weisskopf, V. & Wigner, E. Berechnung der natürlichen Linienbreite auf Grund der Diracschen Lichttheorie. *Z. Phys.* **63**, 54–73 (1930).
2. Purcell, E. M. Spontaneous emission probabilities at radio frequencies. *Phys. Rev.* **69**, 681 (1946).
3. Haroche, S. & Kleppner, D. Cavity quantum electrodynamics. *Phys. Today* **42**, 24–30 (1989).
4. Pelton, M. Modified spontaneous emission in nanophotonic structures. *Nat. Photonics* **9**, 427–435 (2015).
5. Noda, S., Fujita, M. & Asano, T. Spontaneous-emission control by photonic crystals and nanocavities. *Nat. Photonics* **1**, 449–458 (2007).
6. Lalanne, P., Yan, W., Vynck, K., Sauvan, C. & Hugonin, J. P. Light interaction with photonic and plasmonic resonances. *Laser Photonics Rev.* **12**, 1700113 (2018).
7. Liu, Y. M. & Zhang, X. Metamaterials: a new frontier of science and technology. *Chem. Soc. Rev.* **40**, 2494–2507 (2011).
8. Ma, R. M. & Oulton, R. F. Applications of nanolasers. *Nat. Nanotechnol.* **14**, 12–22 (2019).
9. Lodahl, P., Mahmoodian, S. & Stobbe, S. Interfacing single photons and single quantum dots with photonic nanostructures. *Rev. Mod. Phys.* **87**, 347 (2015).
10. Ding, S. Y. et al. Nanostructure-based plasmon-enhanced Raman spectroscopy for surface analysis of materials. *Nat. Rev. Phys.* **1**, 16021 (2016).
11. Deng, F. G., Ren, B. C. & Li, X. H. Quantum hyperentanglement and its applications in quantum information processing. *Sci. Bull.* **62**, 46–68 (2017).
12. Lodahl, P. et al. Chiral quantum optics. *Nature* **541**, 473–480 (2017).
13. Rayleigh, J. W. S. The problem of the whispering gallery. *Philos. Mag.* **20**, 1001 (1910).
14. Rayleigh, J. W. S. *The Theory of Sound* (Dover, 1945).
15. Bender, C. M. & Boettcher, S. Real spectra in non-Hermitian Hamiltonians having PT symmetry. *Phys. Rev. Lett.* **80**, 5243–5246 (1998).
16. Bender, C. M., Boettcher, S. & Meisinger, P. N. PT-symmetric quantum mechanics. *J. Math. Phys.* **40**, 2201–2229 (1999).
17. Guo, A. et al. Observation of PT-symmetry breaking in complex optical potentials. *Phys. Rev. Lett.* **103**, 093902 (2009).
18. Rüter, C. E. et al. Observation of parity–time symmetry in optics. *Nat. Phys.* **6**, 192–195 (2010).
19. Regensburger, A. et al. Parity-time synthetic photonic lattices. *Nature* **488**, 167–171 (2012).
20. Peng, B. et al. Loss-induced suppression and revival of lasing. *Science* **346**, 328–332 (2014).
21. Hodaei, H., Miri, M.-A., Heinrich, M., Christodoulides, D. N. & Khajavikhan, M. Parity-time-symmetric microring lasers. *Science* **346**, 975–978 (2014).
22. Feng, L., Wong, Z. J., Ma, R.-M., Wang, Y. & Zhang, X. Single-mode laser by parity–time symmetry breaking. *Science* **346**, 972–975 (2014).
23. Cao, H. & Wiersig, J. Dielectric microcavities: model systems for wave chaos and non-Hermitian physics. *Rev. Mod. Phys.* **87**, 61 (2015).
24. Feng, L., El-Ganainy, R. & Ge, L. Non-Hermitian photonics based on parity–time symmetry. *Nat. Photonics* **11**, 752–762 (2017).
25. El-Ganainy, R. et al. Non-Hermitian physics and PT symmetry. *Nat. Phys.* **14**, 11–19 (2018).
26. Miri, M. A. & Alù, A. Exceptional points in optics and photonics. *Science* **363**, eaar7709 (2019).
27. Özdemir, S. K., Rotter, S., Nori, F. & Yang, L. Parity-time symmetry and exceptional points in photonics. *Nat. Mater.* **18**, 783–798 (2019).
28. Dembowski, C. Experimental observation of the topological structure of exceptional points. *Phys. Rev. Lett.* **86**, 787 (2001).
29. Heiss, W. D. Exceptional points of non-Hermitian operators. *J. Phys. A* **37**, 2455–2464 (2004).
30. Wiersig, J. Enhancing the sensitivity of frequency and energy splitting detection by using exceptional points: application to microcavity sensors for single-particle detection. *Phys. Rev. Lett.* **112**, 203901 (2014).
31. Berry, M. V. Physics of non-hermitian degeneracies. *Czech. J. Phys.* **54**, 1039–1047 (2004).
32. Pick, A. et al. General theory of spontaneous emission near exceptional points. *Opt. Express* **25**, 12325–12348 (2017).
33. Hernandez, E., Jauregui, A. & Mondragon, A. Jordan blocks and Gamow-Jordan eigenfunctions associated with a degeneracy of unbound states. *Phys. Rev. A* **67**, 022721 (2003).
34. Okołowicz, J., Płoszajczak, M. & Rotter, I. Dynamics of quantum systems embedded in a continuum. *Phys. Rep.* **374**, 271 (2003).
35. Tureci, H. E., Ge, L., Rotter, S. & Stone, A. D. Strong interactions in multimode random lasers. *Science* **320**, 643–646 (2008).
36. Ge, L., Chong, Y. D. & Stone, A. D. Steady-state ab initio laser theory: generalizations and analytic results. *Phys. Rev. A* **82**, 063824 (2010).
37. Milonni, P. W. *The Quantum Vacuum* (Academic, 1994).
38. Lin, Z. et al. Unidirectional invisibility induced by PT-symmetric periodic structures. *Phys. Rev. Lett.* **106**, 213901 (2011).
39. Feng, L. et al. Experimental demonstration of a unidirectional reflectionless parity–time metamaterial at optical frequencies. *Nat. Mater.* **12**, 108–113 (2013).
40. Ge, L., Chong, Y. D. & Stone, A. D. Conservation relations and anisotropic transmission resonances in one-dimensional PT-symmetric photonic heterostructures. *Phys. Rev. A* **85**, 023802 (2012).
41. Peng, B. et al. Chiral modes and directional lasing at exceptional points. *Proc. Natl Acad. Sci. USA* **113**, 6845–6850 (2016).
42. Miao, P. et al. Orbital angular momentum microlaser. *Science* **353**, 464–467 (2016).
43. Wang, X.-Y., Chen, H.-Z., Li, Y., Li, B. & Ma, R.-M. Microscale vortex laser with controlled topological charge. *Chin. Phys. B* **25**, 124211 (2016).
44. Longhi, S. & Della Valle, G. Optical lattices with exceptional points in the continuum. *Phys. Rev. A* **89**, 053132 (2014).
45. Ge, L. Non-Hermitian lattices with a flat band and polynomial power increase. *Photonics Res.* **6**, A10–A17 (2018).
46. Wiersig, J. et al. Nonorthogonal pairs of copropagating optical modes in deformed microdisk cavities. *Phys. Rev. A* **84**, 023845 (2011).

47. Yang, Z. et al. Topological acoustics. *Phys. Rev. Lett.* **114**, 114301 (2015).
48. Ma, G., Xiao, M. & Chan, C. Topological phases in acoustic and mechanical systems. *Nat. Rev. Phys.* **1**, 281–294 (2019).
49. Jiang, X., Li, Y., Liang, B., Cheng, J. C. & Zhang, L. Convert acoustic resonances to orbital angular momentum. *Phys. Rev. Lett.* **117**, 034301 (2016).
50. Shi, C., Dubois, M., Wang, Y. & Zhang, X. High-speed acoustic communication by multiplexing orbital angular momentum. *Proc. Natl Acad. Sci. USA* **114**, 7250–7253 (2017).
51. Zhu, X. F., Ramezani, H., Shi, C. Z., Zhu, J. & Zhang, X. PT-symmetric acoustics. *Phys. Rev. X* **4**, 031042 (2014).
52. Fleury, R., Sounas, D. & Alù, A. An invisible acoustic sensor based on parity–time symmetry. *Nat. Commun.* **6**, 5905 (2015).
53. Liu, T., Zhu, X., Chen, F., Liang, S. & Zhu, J. Unidirectional wave vector manipulation in two-dimensional space with an all passive acoustic parity-time-symmetric metamaterials crystal. *Phys. Rev. Lett.* **120**, 124502 (2018).
54. Padgett, M., Courtial, J. & Allen, L. Light's orbital angular momentum. *Phys. Today* **57**, 35–40 (2004).
55. Yao, A. M. & Padgett, M. J. Orbital angular momentum: origins, behavior and applications. *Adv. Opt. Photonics* **3**, 161–204 (2011).
56. Rodriguez-Fortuño, F. J. et al. Near-field interference for the unidirectional excitation of electromagnetic guided modes. *Science* **340**, 328–330 (2013).
57. Petersen, J., Volz, J. & Rauschenbeutel, A. Chiral nanophotonic waveguide interface based on spin-orbit interaction of light. *Science* **346**, 67–71 (2014).

Methods

Experimental set-up. The microwave cavity is made of stainless steel and consists of a bottom base and a cover, as shown in Fig. 2c,d. The radii of the central metal cylinder and the cavity are 20 mm and 60 mm, respectively. The height of the cavity is 21 mm. The thicknesses of the germanium ridges and air grooves used for refractive index modulation are both 2 mm. In the experiment, we employ a microwave vector network analyser to excite an antenna (fixed within the cavity) as a source to excite the cavity field. The input power is set to be 5 mW. The spectral scanning step is 1 MHz, and the intermediate frequency bandwidth is 50 kHz. The excitation frequency is in the range of 8.150–8.270 GHz. We probe the excited field with another antenna (2 mm length) fixed on an alumina plate above the cavity. The relative position of the probe antenna (fixed on the alumina plate) to the microwave cavity can be tuned by an *XYZ* translation stage placed at the bottom. The spatial scanning steps in the azimuthal direction and radial direction are set to be 1 mm and 2 mm, respectively. The excitation antenna is along the azimuthal direction since the electric field component along the azimuthal direction (E_φ) is dominant inside the cavity. In the vicinity of the alumina plate, only the E_z field (electric field component perpendicular to the alumina plate) exists due to the continuity requirements, and therefore we measure the E_z field in our experiment. Note that the E_z field has a phase shift of $\pi/2$ with respect to the E_φ field (Supplementary Fig. 8). The antennas are made of coaxial cable. The outer conductor and sheath at the end of the cable are stripped away, leaving the centre conductor exposed (the diameter and the length are 0.9 mm and 11 mm, respectively).

For experimental measurements in the acoustic wave system, as shown in Supplementary Fig. 16, the lock-in amplifier (Zurich Instruments HF2LI) sends a continuous sinusoidal signal to the balanced armature (Knowles CI-22955) embedded at the bottom of the cavity. The operating frequency sweeps from 950 to 1,150 Hz, covering the first-order cavity resonant frequency, 1,040 Hz. The vent of the balanced armature is about 1 mm in diameter, much smaller than the wavelength (~331.3 mm at 1,040 Hz), and serves as a monopole source. The generated sound field inside the cavity is measured point by point with an azimuthal step of 10° using a 1/4-inch microphone (Brüel & Kjær type 4935), during which the microphone itself forms part of the wall (that is, it works as a pressure-field microphone) and other holes on the upper cover are sealed using plugs (Supplementary Fig. 16b). The signal is then recorded by the lock-in amplifier after going through a conditioning amplifier (Brüel & Kjær, NEXUS Type 2693A). Here the electrical signal applied to the balanced armature is used as a reference signal to calibrate the phase response. At the bottom of the cavity, a series of slots (azimuthal spacing 15°) is reserved to install the balanced armature (Supplementary Fig. 16c) so that different source positions can be considered.

Numerical mode simulations. We use the commercial software COMSOL Multiphysics to carry out the full-wave simulation throughout this work. In the simulation of the electromagnetic field, the metal is assumed to be a perfect electric conductor. For germanium material, the relative dielectric constant and the electrical conductivity are set to be 16.3 and 2.13 S m^{-1}, respectively. The thicknesses of the germanium ridges and air grooves are both 2 mm. The simulation shows that there only exists one pair of WGM modes at 8.208 GHz in the frequency range of 8.150–8.270 GHz. The electric field distribution of this cavity mode is shown in Supplementary Fig. 8. This result justifies our neglect of other cavity modes with different angular momentums and radial quantum numbers. In the acoustic wave simulation, the background medium is air (22.5 °C, one standard atmospheric pressure) with density $\rho_0 = 1.194\,\mathrm{kg\,m^{-3}}$ and speed of sound $c_a = 344.6\,\mathrm{m\,s^{-1}}$. Other geometrical and material properties of the acoustic ring cavity include the following: cross-sectional area $a \times b = 25 \times 50\,\mathrm{mm^2}$, inner radius $r_{R1} = 40$ mm, outer radius $r_{R2} = 65$ mm, subwavelength periodic grooves with $w = 3\pi/200$ rad, $p = \pi/40$ rad, $h = 5$ mm and $b_{RM} = 29$ mm, and open-back impedance boundaries with $Z_{mpp} = (8.4 + i0.4)\rho_0 c_a$ and $b_{IM} = 9.1$ mm (Supplementary Sections 10 and 11).

Data availability

The data represented in Figs. 2–6 are available as Source Data. All other data that support the plots within this paper and other findings of this study are available from the corresponding author on reasonable request.

Acknowledgements

This work is supported by NSFC under project Nos. 11774014, 91950115, 11574012 and 61521004, Beijing Natural Science Foundation (Z180011) and the National Key R&D Programme of China (2018YFA0704401). J.Z. is supported by the Early Career Scheme of Hong Kong RGC (grant no. PolyU 252081/15E) and the National Natural Science Foundation of China (grant no. 11774297). L.G. is supported by NSF under grant no. PHY-1847240. L.L. is supported by the National Key R&D Programme of China under grant nos 2017YFA0303800 and 2016YFA0302400 and by NSFC under project no. 11721404. R.-J.L. is supported by NSFC under project no. 11974415. X.-F.Z. acknowledges financial support from the National Natural Science Foundation of China (grant nos 11674119, 11690030 and 11690032) and the Bird Nest Plan of HUST.

Author contributions

R.-M.M. conceived the concept and supervised the project. H.-Z.C., X.-Y.W. and R.-M.M. performed the coupled-mode equation analysis and conducted the electromagnetic simulation. H.-Y.L., Y.-B.L., R.-J.L., L.L. and R.-M.M. carried out the microwave experiments. H.-Y.L. and R.-M.M. did the data analysis of the microwave experiment. J.Z. and R.-M.M. initiated the acoustic experiment. T.L., H.-Z.C. and X.-F.Z. performed the simulation and designed the acoustic experiment. T.L., Z.-M.G., S.-J.L. and H.G. conducted the acoustic experiments. T.L., X.Z. and R.-M.M. did the data analysis of the acoustic experiment. J.Z. supervised the acoustic experiment. L.G. performed the Green function and Jordan vector analysis. R.-M.M., H.-Z.C., L.G., T.L., J.Z., X.-Y.W. and S.Z. wrote the manuscript.

Competing interests

The authors declare no competing interests.

Additional information

Supplementary information is available for this paper at https://doi.org/10.1038/s41567-020-0807-y.

Correspondence and requests for materials should be addressed to L.G., J.Z. or R.-M.M.

Peer review information *Nature Physics* thanks Andrea Alu, Nicolas Bachelard, Romain Fleury and Stefan Rotter for their contribution to the peer review of this work.

Reprints and permissions information is available at www.nature.com/reprints.